The coreceptor CD4 is expressed in distinct nanoclusters and does not colocalize with T-cell receptor and active protein tyrosine kinase p56lck

Kyung-Ho Roh[a,b,1], Björn F. Lillemeier[b,c], Feng Wang[a,b], and Mark M. Davis[a,b,2]

[a]The Howard Hughes Medical Institute and [b]Department of Microbiology and Immunology, Stanford University School of Medicine, Stanford, CA 94305; and [c]Salk Institute for Biological Studies, La Jolla, CA 92037

Contributed by Mark M. Davis, February 20, 2015 (sent for review December 15, 2014; reviewed by Balbino Alarcón and Facundo D. Batista)

CD4 molecules on the surface of T lymphocytes greatly augment the sensitivity and activation process of these cells, but how it functions is not fully understood. Here we studied the spatial organization of CD4, and its relationship to T-cell antigen receptor (TCR) and the active form of Src kinase p56lck (Lck) using single and dual-color photoactivated localization microscopy (PALM) and direct stochastic optical reconstruction microscopy (dSTORM). In nonactivated T cells, CD4 molecules are clustered in small protein islands, as are TCR and Lck. By dual-color imaging, we find that CD4, TCR, and Lck are localized in their separate clusters with limited interactions in the interfaces between them. Upon T-cell activation, the TCR and CD4 begin clustering together, developing into microclusters, and undergo a larger scale redistribution to form supramolecluar activation clusters (SMACs). CD4 and Lck localize in the inner TCR region of the SMAC, but this redistribution of disparate cluster structures results in enhanced segregation from each other. In nonactivated cells these preclustered structures and the limited interactions between them may serve to limit spontaneous and random activation events. However, the small sizes of these island structures also ensure large interfacial surfaces for potential interactions and signal amplification when activation is initiated. In the later activation stages, the increasingly larger clusters and their segregation from each other reduce the interfacial surfaces and could have a dampening effect. These highly differentiated spatial distributions of TCR, CD4, and Lck and their changes during activation suggest that there is a more complex hierarchy than previously thought.

coreceptor CD4 | T-cell receptor | superresolution microscopy | PALM | dSTORM

For helper T cells, CD4 has been termed a coreceptor based on its important role in antigen recognition class II major histocompatibility complex (MHC)–peptide complexes by the αβ T-cell receptor (TCR) as well as in signal transduction. Indeed, CD4 significantly increases T-cell sensitivity to antigen upon activation (1–4). This ability of CD4 to enhance antigen recognition has often been connected to the fact that the N-terminal Ig domain of CD4 has specific affinity to invariant sites on MHC class II molecules (5, 6). It has been suggested that CD4 stabilizes the molecular complex of TCR and peptide–MHC (pMHC) by binding to the same MHC either simultaneously with the TCR (7) or shortly after TCR–pMHC engagement (2, 3). However, from more recent 2D measurements, CD4 blockades showed no effect on the stability of TCR binding to agonist peptide–MHC complexes in a synapse (8). In terms of signal transduction, the role of CD4 has been studied based on the binding ability of a cysteine motif in the cytoplasmic tail of CD4 to Src kinase p56lck (Lck) (9), which is responsible for the phosphorylation of the immunoreceptor tyrosine-based activation motif (ITAM) sequences in TCR–CD3 complex as the earliest observable biochemical event during T-cell activation (10). It has been proposed that CD4 mainly contributes to the sensitivity of T cells by facilitating the recruitment of Lck to TCR–CD3s that are actively engaged in ligand recognition (11, 12). Nevertheless, the absence of CD4 does not preclude T cells from being generated at the thymus or being activated by TCR–pMHC engagement (13, 14).

It is now well appreciated that spatial reorganization and distribution of some of the membrane receptors and signaling molecules is one of the critical regulating mechanisms in T-cell activation. The molecular assembly and clusters such as supramolecular activation clusters (SMACs) (15) of immunological synapse (IS) (14), microclusters (16–20), and their roles in T-cell signaling have been widely studied. More recently, the presence and unique roles of smaller-sized protein clusters, termed "nanoclusters" or "protein islands," of TCR–CD3 complex (21–24), linker for activation of T cell (LAT) (21, 22, 24, 25), Lck (26), and other signaling molecules (24) were revealed by electron microscopy and the newly available superresolution fluorescence microscopy.

Considering that the TCR–CD3 complex, CD4, and Lck are constitutively expressed in nonactivated T cells, it is highly likely that the interaction dynamics between these components would also be controlled spatially during the T-cell activation process. Here, we studied the relative molecular distribution of these molecules using single- and dual-color photoactivated localization

Significance

Immune cell signaling is heavily associated with the spatial organization of molecules. Here, we examined the nanoscale organization of coreceptor CD4 and its relative spatial localization to the T-cell receptor and the active form of Src kinase p56lck (Lck), using two different superresolution microscopy techniques photoactivated localization microscopy and direct stochastic optical reconstruction microscopy in both living and fixed cells. With concurrent spatial analyses, we show that neither CD4/T-cell antigen receptor nor CD4/active Lck nanoclusters colocalize but only overlap at the interfaces. In activated T cells, the enhanced clustering of each kind results in increased seclusion from each other. Our observations here in molecular resolution may reveal the general roles that are played by nanoscale organization of critical components in immune cell signaling.

Author contributions: K.-H.R. and M.M.D. designed research; K.-H.R. performed research; B.F.L. and F.W. contributed new reagents/analytic tools; K.-H.R. analyzed data; K.-H.R. and M.M.D. wrote the paper; and B.F.L. contributed to the initial setup of microscopy.

Reviewers: B.A., Consejo Superior de Investigaciones Cientificas; and F.D.B., Cancer Research UK.

The authors declare no conflict of interest.

Freely available online through the PNAS open access option.

[1]Present address: Department of Biomedical Engineering, Georgia Institute of Technology, Atlanta, GA 30332.

[2]To whom correspondence should be addressed. Email: mmdavis@stanford.edu.

This article contains supporting information online at www.pnas.org/lookup/suppl/doi:10.1073/pnas.1503532112/-/DCSupplemental.

microscopy (PALM) (27) and direct stochastic optical reconstruction microscopy (dSTORM) (28, 29) in live and fixed T cells for both nonactivated and activating conditions. The corresponding spatial analyses were also used to quantitatively determine the sizes, degree of clustering, and degree of interactions of these clusters. We found that CD4 is also expressed in preclustered structures, separate from TCR–CD3 and LAT, and composed of three to six molecules per cluster. The interactions between these molecules occurred only in the interfaces between the clusters. Upon T-cell activation, the TCR–CD3 and CD4 molecules increased the size of their own clusters without appreciable mixing. Instead, their molecular segregation increased, whereas the T cell develops a synapse structure, often in the SMAC or "bull's eye" pattern, with the TCR–CD3 in the central supramolecular activation cluster (cSMAC) with the CD4 and Lck clusters localizing around it. These observed clustering behaviors accompanying reorganization of spatial distributions of CD4, Lck, and TCR might be a general and effective mechanism to activate and regulate the T-cell signaling by controlling the magnitude of interfacial interactions between signaling components in each cluster.

Results

CD4 Molecules Exist in Nanoclusters and Concatenate/Merge upon Activation of T Cells. To determine the molecular distribution of CD4 at the intact T-cell plasma membrane, we used a superresolution fluorescence microscopy technique, PALM. We cloned murine CD4 fused to the photoconvertible fluorescent proteins PSCFP2 (30) or photoactivatable fluorescent proteins PAmCherry (31) at the CD4 C terminus (Fig. S1*A*) and expressed them in the plasma membranes of murine primary T-cell blasts prepared from the lymph nodes of 5c.c7 TCR-transgenic mice by retroviral transduction. These T cells are specific for the major histocompatibility complex class II molecule IE^k presenting the moth cytochrome *c* 88–103 peptide (IE^k–MCC) (32). Using both fluorescent protein tags, we could produce statistically evaluable data with a positional accuracy of 20–50 nanometers from the imaging of live T cells for 5- to 10-s data acquisition durations. We analyzed CD4–PSCFP2 or CD4–PAmCherry molecules expressed in plasma membrane of T cells sitting on either a nonactivating surface (poly-L-lysine, PLL) or an activating surface [IE^k–MCC plus B7.1 (CD80)]. The T cells spread over 5–12 μm in width on nonactivating surfaces and were 8–18 μm in width on activating surfaces. Their activation status was confirmed by Ca^{2+} flux measurements (Fig. S2).

We reconstituted the superresolution images as probability density plots of the tagged molecules (Fig. 1*A*), and used Ripley's *K* function for quantitative spatial analyses (Fig. 1 *B*–*D*). As previously reported for TCR–CD3 (21), Lat (21, 24, 25), and Lck (26), CD4 was not randomly distributed in nonactivated cells but preclustered in nanometer-scale membrane compartments (Fig. 1*B*). By comparing the maxima of L(*r*) minus *r* in Ripley's *K*-function analysis (nonactivated: 36.3 ± 14.5 and activated: 72.7 ± 24.9), we observed that the degree of clustering is enhanced upon T-cell activation (Fig. 1 *B* and *C*). The r_{max} value where L(*r*) minus *r* has a maximum value is indicative of the sizes of the analyzed clusters. The r_{max} values also grow from 355 ± 178 nm in nonactivated state to 529 ± 216 nm in activated state (Fig. 1*D*). Thus, we could conclude that there is a significant increase in clustering of CD4 after activation, compared with the nonactivated condition.

We also calculated the fraction of CD4 molecules that have at least one neighboring molecule within varying distances. The values from the PALM experiments showed positive deviation from the values calculated for the randomized case (Monte Carlo method) for distances up to ~85–95 nm, regardless of the activation status (Fig. S3). This distance could be interpreted as a radius of a hypothetically circular nanocluster, and 94–97% of the detected molecules were found within a cluster of this size. The number of CD4 molecules within a cluster increased from 4–8 in the nonactivated state to 6–15 in the activated state (*Materials and Methods*). Whether this increase in molecular density results from a mere concatenation of noncircular nanoclusters or a merging of multiple clusters is not clear (Fig. S4). Nevertheless, the increase in number of molecules for similar clustering distances before and after activation further support the increase in clustering of CD4 molecules upon T-cell activation.

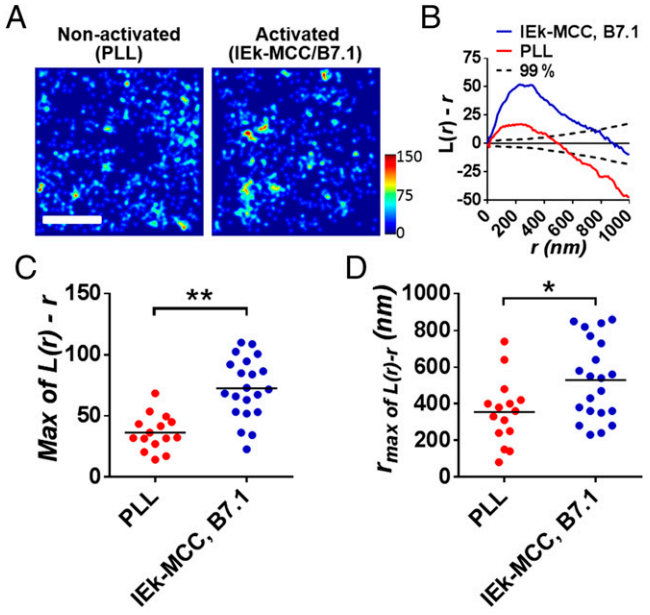

Fig. 1. Analysis of the spatial distribution of CD4 in live T-cell membranes by PALM. (*A*) Colormap probability density plots for CD4–PSCFP2 expressed in live T cells interfacing with nonactivating (PLL, *Left*) and activating (IE^k–MCC and B7.1, *Right*) immobilized surfaces. (Scale bar, 1 μm.) Color bar scale represents the relative molecular density. (*B*) Ripley's *K*-function plot of CD4–PSCFP2 molecules on a nonactivated (red solid line) or an activated (blue solid line) surface with a 99% confidence interval (black dashed line). Peaks of Ripley's *K*-function plots were analyzed for the maxima values of L(*r*) − *r* (*C*) and r_{max} (*D*) for multiple cells (n = 15 and 21 for nonactivating and activating condition, respectively). *P < 0.01 and **P < 0.0001 (Student t test). Data are representative (*A* and *B*) and collections (*C* and *D*) of experiments for the selected areas of 3 × 3 μm^2, in total 28 cells.

Dual-Color PALM Shows Limited Interactions Between CD4 and TCR in both Nonactivated and Activated T Cells. We first used dual-color PALM to study the relative spatial organization of CD4 and TCR (labeled for CD3ζ in dual-color PALM experiments) in live T cells. Using a 2A-like peptide sequence (T2A) (33, 34) within a murine stem cell retroviral vector (Fig. S1*B*), both chimeric proteins, CD3ζ–PSCFP2 and CD4–PAmCherry, were simultaneously expressed in the plasma membrane of the same primary 5c.c7 T blast. Using a beam splitter that allows the simultaneous acquisition of two colors in different regions of a CCD camera, we could achieve dual-color imaging within 10 s of acquisition with mean positional accuracies of 31 and 28 nm for PSCFP2 and PAmCherry, respectively (Fig. S5). For nonactivated and activated T cells, the superresolution images of green (CD3ζ) and red (CD4) channels are reconstituted as probability density plots and precise overlay of the two channels with the appropriate color codes yielded two-color PALM images (Fig. 2*A*). We could first qualitatively determine the spatial distributions by close examination of these two-color images (such as zoomed images of 1 × 1 μm^2 *Insets* in Fig. 2*A*). In nonactivated cells, the TCR and CD4 molecules reside in separate nanoclusters that are

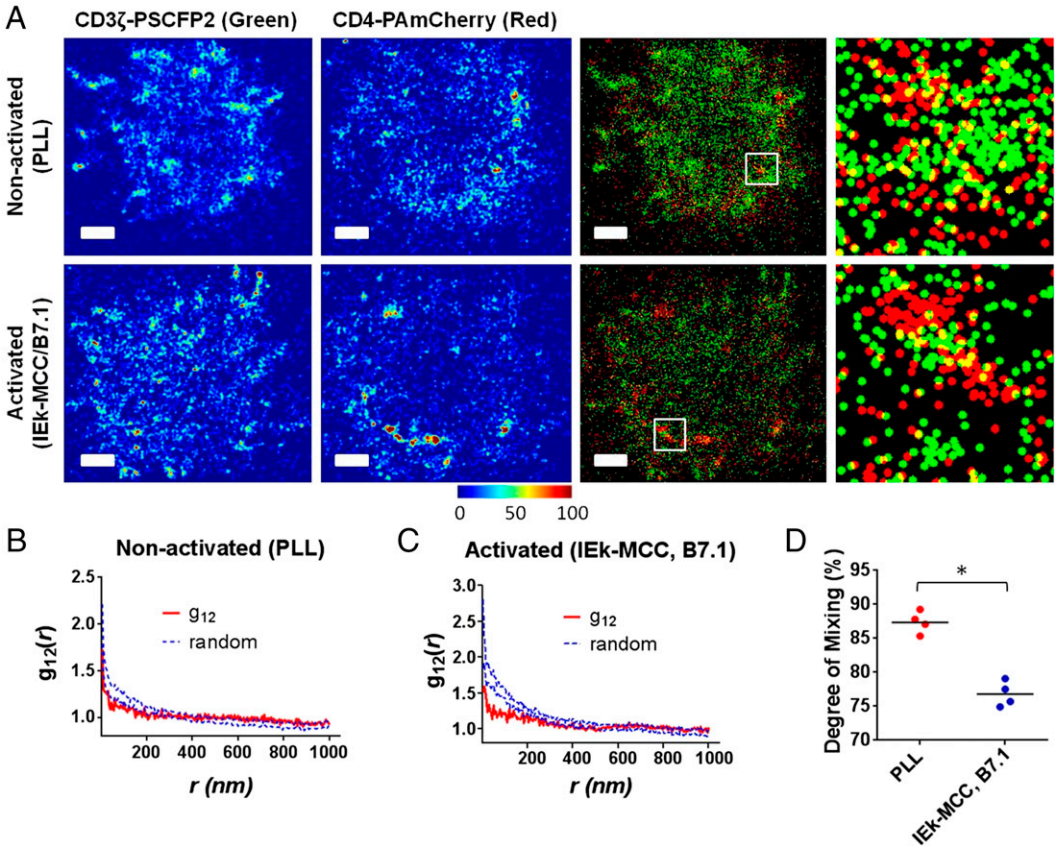

Fig. 2. Analysis of relative spatial distribution of CD4 and TCR in live T-cell membranes by dual-color PALM. (*A*) Dual-color PALM images for CD3ζ–PSCFP2 (green) and CD4–PAmCherry (red) coexpressed in live T cells interfacing nonactivating (PLL, *Left*) and activated (IE^k–MCC and B7.1, *Right*) immobilized surfaces. Each color map represents the probability density distribution image of each fluorescence channel. Color bar scale represents the relative molecular density. Enlarged dual-color PALM images are 1×1 μm^2 areas of white *Inset* squares. (Scale bar, 1 μm.) (*B* and *C*) Bivariate pair-correlation function curves (red solid lines) of CD3ζ and CD4 on nonactivating (*B*) and activating (*C*) conditions. Blue dashed lines indicate 95% confidence intervals of a random labeling (100 Monte Carlo simulations). (*D*) The degree of mixing parameter between CD3ζ and CD4 (as defined in the text and *Materials and Methods*) compared between nonactivating and activating conditions for multiple cells ($n = 4$ for both conditions). *$P < 0.0001$ (Student t test). Data in *A*–*C* are representative of experiments for a total of 18 cells. Only the cells with the representative 3×3 μm^2 areas where both molecules were detected at densities bigger than 100 molecules per square micrometer were used for the determination of the degree of mixing parameter (*D*).

composed of 4–8 molecules and 13–18 molecules for CD4 and TCR–CD3, respectively. The interaction between TCR and CD4 (depicted as yellow dots in the two-color images) seems to be limited to the interfaces between their clusters. In activated T cells, the concatenations of these nanoclusters occur without further molecular interaction between the TCR and CD4, which in turn yields enhanced segregation from each other.

These findings could also be confirmed by quantitative analyses. We first calculated the fraction of CD4 molecules that have at least one neighboring TCR–CD3 within varying distances and compared the values calculated from the randomized spatial distributions of both CD4 and TCR–CD3 (Monte Carlo method) (Figs. S6–S8). In the nonactivated state, the PALM data showed positive deviation from the randomized cases, from 0 nm to a range of 25–50 nm, and negative deviations in a distance range of 30–200 nm (Fig. S6). Within the distance ranges showing positive deviations, 49.8 ± 4.8% of total CD4 molecules associate with TCR–CD3 molecules, where one CD4 molecule is in close contact with 2.3 TCR–CD3 molecules on average. These data quantitatively support our finding that only the CD4 molecules on the border of a cluster are in close contact with TCR–CD3 and the molecules inside of a cluster seem to be spatially excluded from this interaction. The same analysis, applied to the activated T cells (Fig. S7), showed statistically equivalent results to the nonactivated T cells (Fig. S8). Next, we used bivariate cross-correlation function analysis (Fig. 2*B*). In this analysis, we compared the bivariate curve [$g_{12}(r)$; Fig. 2*B*, red solid lines] with the 95% confidence interval of a random labeling model (Fig. 2*B*, blue dotted lines). In a nonactivated cell, the curve is just below the confidence interval, which indicates that there is limited interaction between TCR and CD4 molecules. Nevertheless from a statistical point of view, the two molecules are slightly segregated from each other compared with the random labeling. In an activated cell, the displacement of the curve below the confidence interval is much bigger, which suggests an enhanced segregation. To quantify the difference in the amount of segregation of nonactivated and activated T cells, we calculated the ratio between the bivariate correlation curve and mean value of confidence intervals and averaged for these values below 100 nm to introduce "degree of mixing" parameter for multiple individual cells (Fig. 2*C*). The results also confirm that CD4 and TCR are more segregated under activating conditions (degree of mixing ~76%) than in nonactivating conditions (degree of mixing ~87%) compared with the random labeling (100% degree of mixing). Taken together, these data suggest that interaction between CD4 and TCR molecules is limited to those molecules (about 50% of total populations) residing at the interface (35–50 nm) of the different protein islands under both activating and nonactivating conditions.

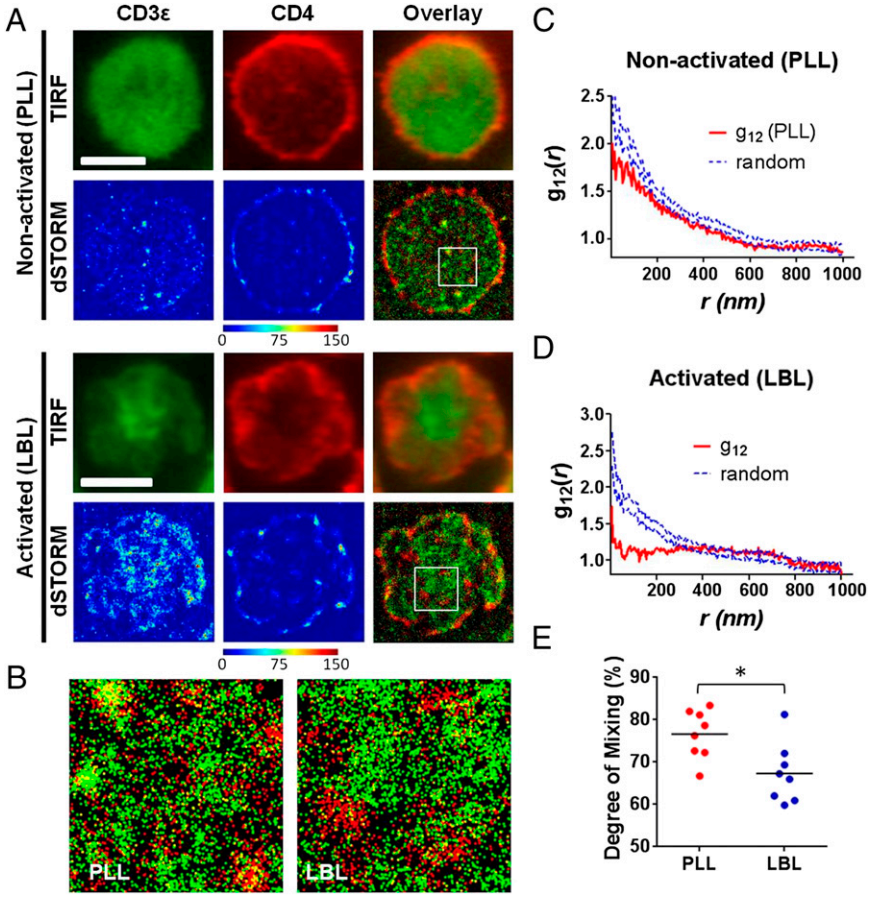

Fig. 3. Analysis of relative spatial distribution of CD4 and TCR by dual-color TIRFM and dSTORM. (*A*) Dual-color TIRFM and dSTORM images of T cells fixed at 10 min after interfacing with nonactivating PLL (*Upper*) or activating LBL (*Lower*) surfaces. The T cells were stained with anti-CD3ε–AF488 (green) and anti-CD4–AF647 (red) antibodies. Each color map in dSTORM data represents the probability density distribution image of each fluorescence channel. Color bar scale represents the relative molecular density. (Scale bar, 5 μm.) (*B*) Enlarged dual-color dSTORM images of 3 × 3 μm^2 areas of white *Inset* squares in *A*. (*C* and *D*) Bivariate pair-correlation function curves (red solid lines) of CD3ε and CD4 on nonactivating (*C*) and activating (*D*) conditions. Blue dashed lines indicate 95% confidence intervals of a random labeling (100 Monte Carlo simulations). (*E*) The degree of mixing parameter between CD3ε and CD4 (as defined in the text and *Materials and Methods*) compared between nonactivating (PLL) and activating (LBL) conditions for multiple cells ($n = 8$ for both conditions). *$P < 0.05$ (Student *t* test). Data in *A*–*D* are representative of experiments for a total of 15 cells. Only the cells with the representative 3 × 3 μm^2 areas where both molecules were detected at densities bigger than 100 molecules per square micrometer were used for the determination of the degree of mixing parameter (*E*).

Dual-Color dSTORM Imaging Confirmed the Limited Association Between CD4 and TCR Nanoclusters in Nonactivated T Cells. The live cell PALM approach is the most noninvasive and physiological superresolution imaging modality owing to the use of genetically encoded fluorescent proteins. However, there still are chances to encounter artifacts that might distort to the molecular organization. For example, the expression of exogenous molecules with fluorescent protein tags could alter the natural expression level or organization of a given molecule. Competition between the endogenous and exogenous molecules and the selective detection of tagged populations might also generate artifacts. Additionally, a significant compromise in resolution can be induced in superresolution live cell imaging due to the spontaneous movements, such as molecular diffusion (35, 36), of the molecules of interest during the acquisition period (37). Therefore, we also performed dSTORM imaging for the nonactivated T blast sitting on PLL (Fig. 3 *A* and *B*). The T cells were fixed and permeabilized, before TCR and CD4 were labeled with fluorophore-conjugated monoclonal antibodies, antiCD3ε–Alexa-Fluor 488 antibody, and anti-CD4–Alexa-Fluor 647 antibody, respectively. As the staining was performed with conventional fluorescent dyes, the diffraction-limited total internal reflection fluorescence microscopy (TIRFM) images could also be acquired before most of the dyes were switched to the dark state for dSTORM acquisition (29) in an identical cell. The seemingly homogeneously distributed TCR (CD3ε for the rest of TIRFM and dSTORM experiments) in the TIRFM image is actually residing in small nanoclusters in reconstructed dSTORM image, as previously seen in the live cell PALM experiments. In TIRFM, CD4 also looked homogeneously distributed with certain local fluctuations of fluorescence signals throughout the membrane, whereas significant accumulation of fluorescent signal was observed in the periphery. However, the dSTORM images also confirm the preclustered nature of CD4 in nonactivated cells (Fig. S9*A*). In Ripley's *K*-function analysis performed for multiple individual cells (Fig. S9 *B* and *C*), the degree of clustering measured by maxima values of L(*r*) minus *r* (50.7 ± 23.3) is bigger than the value measured in PALM. This discrepancy might originate from the difference in labeling and detection of molecules between PALM and dSTORM: Each antibody molecule used in dSTORM contains multiple dye molecules and these dye molecules can reversibly photoswitch for multiple cycles, whereas in PALM, each molecule is genetically tagged with a single fluorescent protein, and the blinking (38) of fluorophores could

be minimized (*Materials and Methods*). However, the r_{max} values, 282 ± 103 nm, which are indicative of the cluster sizes and not affected by the photoswitching behavior of a fluorescent tag or the labeling density, are comparable to the values measured using PALM (Fig. S9*D*). The dual-color dSTORM images (Fig. 3 *A*, *Top* and *B*, *Left*) and bivariate cross-correlation function analyses on those images also yielded results comparable to PALM, showing that clusters of TCR and CD4 are segregated from each other with limited interactions (Fig. 3*C*).

T Cells Activated on Fluid Lipid Bilayers Formed a SMAC and dSTORM Shows That the CD4 Clusters Are Largely Excluded from the Central TCR Clusters. As both TCR and CD4 have affinities toward pMHC molecules, using an activated surface with IE^k–MCC molecules in their fixed positions (i.e., an immobilized surface) might generate artifacts or could potentially hinder the most physiological movements of the molecules upon activation of T cells. To address this issue, we also examined the T-cell membranes activated on fluid lipid bilayers presenting ∼180 IE^k–MCC, ∼20 B7-1, and ∼25 ICAM-1 molecules per square micrometer. On these supported lipid bilayers, the formation of the bullseye pattern with a centrally concentrated TCR cSMAC and the integrin, LFA-1, concentrated in the outer ring (peripheral supramolecular activation complex, pSMAC) is a well known feature of the T-cell IS (14, 15). When we examined the fixed T cells after incubation on the lipid bilayers for 10 min at 37 °C with TIRFM, the majority of the T cells examined (58 of 67, ∼87%) clearly developed a cSMAC structure (Fig. 3*A*, *Bottom*). TIRFM for the CD4 channel and its overlay with the TCR channel showed very minimal overlap with the TCR-concentrated region. This differential clustering of CD4 and TCR was previously shown in the interface between T cells and antigen-presenting cells (APCs) (39).

Again, Ripley's *K*-function analysis for the dSTORM images of CD4 molecules was performed for multiple cells. Here, we observed a clear accumulation of CD4 molecules in the periphery of the cell-surface contact area on both PLL and lipid bilayer (LBL). Because the clustering behaviors were clearly differentiated for the inner area (Fig. S9) versus the periphery (Fig. S10), we analyzed the data separately. For the molecules detected in the inner contact area, both the degree of clustering and the size of the clusters increased compared with nonactivated T cells, similar to live-cell PALM results on an immobilized surface (Fig. S9 *C* and *D*). The r_{max} values measured on lipid bilayers were statistically identical to the values measured on immobilized surfaces. In contrast, the molecules detected in the periphery showed a very wide range in their degree of clustering as well as cluster size, both of which were statistically equivalent for both activated and nonactivated cells (Fig. S10).

In the dual-color dSTORM images, it is noteworthy that most of the CD4 clusters reside outside of the centrally concentrated TCR clusters (Fig. 3*A*, *Bottom*). Even though we could observe the presence of CD4 clusters within the central region of concentrated TCRs, the interaction between the TCR and CD4 clusters was always very minimal. The bivariate cross-correlation analysis confirms this enhanced segregation in this highly organized IS (Fig. 3*D*).

The degree of mixing parameters calculated from dSTORM images for nonactivated cells (mean ∼77%) were about 10% smaller than the values calculated from PALM images. This is again probably due to artifacts originating from the multiple labeling for a single molecule plus potential multiple recognition of a single dye in dSTORM. Nevertheless, the degree of mixing calculated for the cells activated on the lipid bilayers also showed diminished values (mean ∼67%), which indicates that CD4 and TCR clusters further segregate from each other during mature IS and SMAC formations (Fig. 3*E*). Taken together, these data suggest that CD4 clusters are largely excluded from the centrally located TCR clusters in what has been termed a mature immunological synapse (14, 15).

Constitutively "Active" LcK Molecules Reside in Separate Clusters and Accumulate Near the Central Region upon T-Cell Activation, but with only Limited Interactions with TCR and CD4 Clusters. The enzymatic activity of LcK depends on conformational changes regulated by phosphorylation and dephosphorylation of two critical tyrosine residues, Y394 and Y505 (40). Lck molecules show an enhanced substrate phosphorylation only when Y394 is phosphorylated, regardless of phosphorylation status of Y505 (41, 42). And a significant fraction of Lck molecules exist in these "active" forms in both nonactivated and activated T cells (43). So we examined the spatial distribution of these active Lck molecules by TIRF and dSTORM after specific fluorescence labeling with a polyclonal antiserum specific for the Y394 phosphorylation.

First in TIRF imaging, we could observe some clustered structures of Lck molecules in both cases of T cells sitting on PLL and LBL (green channel images in Fig. 4*A*). Compared with TCR or CD4 clusters in T cells on PLL (red images in Fig. 4*A*), which are smaller and barely noticeable in diffraction-limited TIRFM images, we could always detect distinguishable clusters of Lck on PLL. And these clusters of Lck are distributed evenly across the T-cell–PLL surface contact area. Upon the activation of T cells on fluidic bilayers for 10 min, the Lck clusters accumulate near the central region in the T-cell–LBL contact area. It was previously shown that the major interaction between active Lck and TCR is limited to peripheral microclusters after around 5 min of activation (18). The relative macroscopic distributions of Lck molecules with those of TCR and CD4 were compared by the relative intensities of the line scans for green and red TIRFM images for each labeled T cell (Fig. 4*B*). First, both Lck and TCR are evenly distributed across the contact with PLL, and line scans of the Lck channel shows more distinguishable peaks compared with that of TCR, which indicates that the sizes of Lck clusters are bigger than those of TCR. The line scans of CD4 molecules on PLL confirms the accumulation in the periphery of the contact area as described in the previous section and the uniform distribution with a few distinguishable peaks across the contact. The relative spatial distributions of Lck and CD4 on PLL do not correlate well. On bilayer surfaces, line scans of the TCR channel shows a very narrow peak in the central region, which corresponds to the well-known cSMAC. Lck molecules are clearly accumulated near the cSMAC of the major TCR accumulation. However, the distance over which the Lck molecules accumulate is wider than that of TCR, i.e., the accumulation pattern is not as concentrated as that of the TCR. The two peaks in the line scan of Lck locates 1.5 ± 0.1 μm away from the central peak of the TCR cSMAC line scan, which corresponds to the observation of TIRF image where Lck molecules are recruited near to the central region, but only accumulate around the SMAC of TCR. As we observed a similar accumulation of CD4 molecules around the central TCR SMAC described in the previous section, we were curious whether or not Lck and CD4 colocalize around the TCR cluster. The TIRFM images and line scan of CD4 and Lck pair show that both CD4 and Lck clusters accumulate near the central region, but the local peaks do not overlap with each other; that is, the CD4 and Lck clusters seem to be separated from each other.

Next we used dSTORM imaging and the corresponding Ripley's *K*-function analysis to examine the clustering behavior of Lck (Fig. S11 and Fig. 4 *C* and *D*). Regardless of activation status, we observed the Lck molecules reside in clustered structures. And we found that clusters with wide ranges of the degree of clustering and cluster sizes coexist in a single cell (Fig. S11). As a natural consequence, from the analyses of multiple cells, there were no statistically significant changes upon the activation

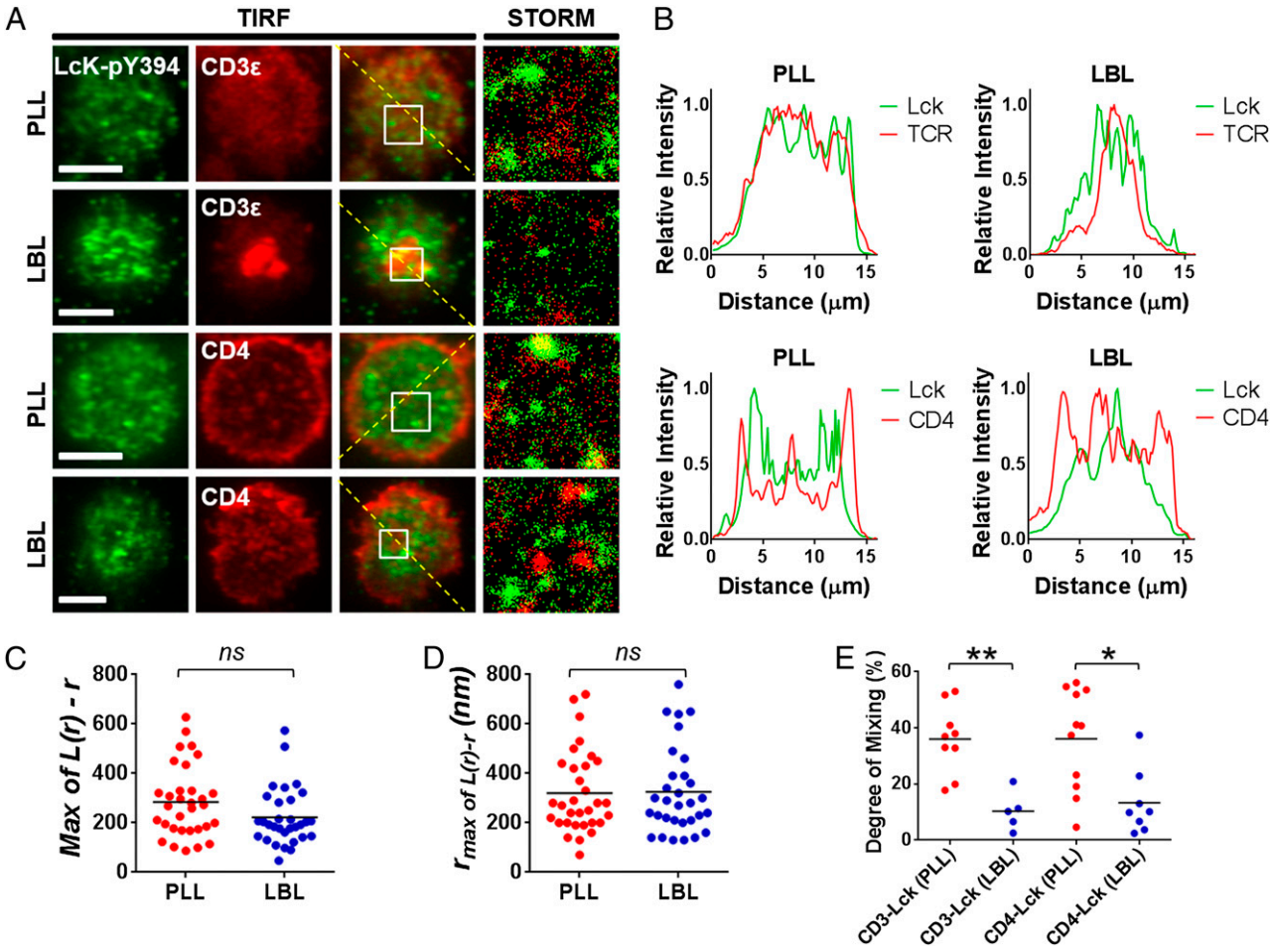

Fig. 4. Analysis of relative spatial distribution of active Lck paired with CD4 or TCR by dual-color TIRFM and dSTORM. (*A*) Dual-color TIRFM (the first three columns from the *Left*) and dSTORM (the fourth column) images of T cells fixed at 10 min after interfacing with nonactivating PLL (the first and third rows from the *Top*) or activating LBL (the second and fourth rows) surfaces. Active Lck molecules were stained with anti-Lck–pY394 antibody (AF488, green) and TCR or CD4 were stained with anti-CD3ε (*Upper* two rows) or anti-CD4 (*Lower* two rows) antibodies (AF647, red). (Scale bar, 5 μm.) Dual-color dSTORM images (the fourth column) are enlarged for 3×3 μm^2 areas of white *Inset* squares in TIRFM images (the third column). (*B*) Relative fluorescence intensities of active Lck (green solid lines) paired with TCR or CD4 (red solid lines) for nonactivating (PLL, *Left* column) and activating (LBL, *Right* column) on the diagonal yellow dashed lines in TIRFM images in *A*. (*C* and *D*) Clustering analysis for the active Lck molecules by Ripley's *K* function. Peaks of Ripley's *K*-function plots (Fig. S11) were analyzed for the maxima values of $L(r) - r$ (*C*) and r_{max} (*D*) for multiple cells ($n = 32$ for PLL, $n = 31$ for LBL). (*E*) The degree of mixing parameter between active Lck and CD3ε and between active Lck and CD4 were compared for nonactivating (PLL) and activating (LBL) conditions from the experiments of multiple cells ($n = 9$ for Lck–CDε on PLL, $n = 5$ for Lck–CDε on LBL, $n = 11$ for Lck–CD4 on PLL, and $n = 8$ for Lck–CD4 on LBL). NS, statistically nonsignificant. $*P < 0.01$ and $**P < 0.001$ (Student *t* test). Data in *A* and *B* are representative of experiments for a total of 33 cells.

of T cells, either in degree of clustering [maximum value of L(*r*) minus *r*, 284.2 ± 143.9 (PLL) vs. 222.1 ± 116.4 (LBL)] or in size of clusters [r_{max}, 320.3 ± 165.3 (PLL) vs. 325.8 ± 175.5 (LBL)], despite the macroscopic reorganization of Lck molecules observed in TIRFM.

Even though the presence of Lck clusters overlaying with either TCR or CD4 clusters was not visible in TIRFM, it is ambiguous with these data to determine what fraction of molecules are in close enough proximity such that they can readily interact. Therefore, we used dual-color dSTORM imaging for the pairs of Lck–TCR and Lck–CD4 (Fig. 4*A*). By analyzing the data with bivariate cross-correlation function, we could quantitatively determine the degree of mixing parameter including those populations of molecules that are residing in small nanoclusters that were not resolved in the diffraction-limited TIRFM (Fig. 4*E*). For both pairs of Lck–TCR and Lck–CD4, the degree of mixing calculated for the nonactivated cells (sitting on PLL) had mean values around 36%, which indicates that the molecules in their separate nanoclusters are already quite secluded from each other compared with the hypothesized random mixing. And again they were even more segregated within the first 10 min of T-cell activation, as indicated by their decreased degree of mixing values [mean values of 10% (Lck–TCR) and 13% (Lck–CD4)]. Thus, we could conclude that the interactions between the active Lck molecules with TCR and CD4 are tightly regulated as the macroscopic spatial reorganization of the nanoclusters progresses to form a mature immunological synapse.

Discussion

Here, we examined the molecular distribution of CD4 in a live T-cell membrane using two different methods of "superresolution" fluorescence microscopy. For the most physiological observation of CD4 distribution in T-cell membrane without generating complications from antibody labeling and cellular fixation, we first used a live-cell PALM approach. If T cells are placed on a nonactivating PLL surface to represent the nonactivated state, CD4 molecules reside in separate protein islands or nanoclusters, as previously shown for TCR–CD3 complexes (21–23),

Lat (21, 22, 25), and Lck molecules (26). On an activating but immobilized surface presenting pMHC and B7.1 molecules to T cells these CD4 clusters concatenate to form bigger and denser microclusters, as seen for other T-cell membrane proteins (21, 24–26).

Because it is known that CD4 molecules bind to peptide MHC complexes in productive complexes with TCR–CD3 complexes, we expected that these CD4 clusters would merge with TCR islands. However, instead, in both PALM and dSTORM experiments, it is clear that these TCR-CD3 and CD4 clusters remain segregated, except at the interface within the limits of positional accuracy (~25 nm) (depicted as yellow pixels in Figs. 2 and 3). This finding is quantitatively supported by cross-correlation function analyses and by the introduction of the degree of mixing parameter, which showed that the determined probability of co-clustering is smaller than the randomized case.

For dual-color imaging of TCR–CD4 pairs in activated T-cell membranes, we presented physiological agonist pMHC with B7.1 either on immobilized glass slides or on glass-supported fluid lipid bilayers in PALM or dSTORM, respectively. Regardless of the fluidity of the activating surfaces, the separate concatenations of TCR and CD4 clusters result in further segregation. The T cells developed highly concentrated TCR clusters in the central region of T-cell–LBL contact as a well-defined cSMAC. In diffraction-limited TIRFM images, these cSMAC of TCR looked like a single entity. It was previously shown that the cSMAC is formed by a collection of microclusters that are transported from the periphery (17, 18), and that these microclusters maintain their independent movement before they fuse to form larger clusters and become immobilized in an interconnected network between 5 and 15 min after the initiation of activation (44). In our dSTORM images, the cSMAC is composed of multiple concatenated microclusters of TCR. Interestingly, we could often observe a smaller number of separate CD4 microclusters intercalated within the larger number of TCR clusters. However, importantly, the majority of CD4 microclusters aligned along the periphery of cSMAC of TCR (Fig. 3). This finding agrees well with the disparate spatial accumulation and segregation of CD3ζ and CD4 at the IS formed between T-cell–APC interfaces (39, 45), but with a much higher resolution than previously reported.

The spatial distribution of TCR–CD3 and CD4 was previously examined using another nondiffraction-limited optical microscopy technique, namely near-field scanning optical microscopy and immune-labeling quantum dots (46). In their best resolution of around 50 nm, the authors showed that the TCR–CD3 and CD4 reside in their separate nanoclusters with minimal association in a nonactivated state, which agrees well with our findings. However, they found significant colocalization of TCR–CD3 and CD4 when the T cells were imaged after being activated on an anti-CD3 antibody-coated surface for 8 h and fixed. The degrees of clustering of TCR–CD3 and CD4 as well as their colocalization were enhanced by an addition of anti-CD28 antibody in their 8-h activation culture. For a direct comparison, our live cell PALM data acquired on a glass slide coated with immobilized pMHC with B7.1 would be the most similar counterpart, for they also used an immobilized surface for the activation of T cells. However, it is difficult to know what caused the discrepancy due to the many differences in the experimental designs including T-cell source (mouse T blast vs. Rhesus monkey peripheral naïve T cells), activation method (pMHC with B7.1 vs. anti-CD3 and anti-CD28 antibodies), duration of activation (~5–15 min vs. 8 h), or simply the resolution.

To fully interpret the implications of the findings in the relative spatial organization of TCR and CD4, it was required to examine their relative spatial distributions with Lck, one of the main and probably the most initial kinases for phosphorylation of ITAM motifs in CD3 upon TCR–pMHC engagement. And there is accumulating evidence that supports the common postulation that CD4 contributes to T-cell function by recruiting Lck (11, 12, 47, 48). The recruitment of Lck by CD4 could be divided to two steps: the first step is the recruitment of Lck toward the IS formed between the T cell and APC, and the second step is the spatial recruitment of Lck to its substrate TCR–CD3 complexes within the T-cell–APC interface. The first recruitment was directly observed for the Lck molecules accumulated in the IS (11, 12, 39, 45). However, the second recruitment of Lck molecules to TCR–CD3 complexes is less studied and the role of CD4 in this recruitment is still elusive. Furthermore, it has only recently become clear that all four different conformational states of Lck are determined by the combined phosphorylation status of two regulating tyrosine residues (Y394 and Y505) and that these constitutively coexist in a dynamic equilibrium, regardless of the activation status of a T cell (43, 49). However, it is not as clear whether or not the activation of a T cell induces changes in the relative proportions of the activated forms of Lck (43, 50). Therefore, how nonspecific phosphorylation of the ITAM motif by constitutively existing active forms of Lck is regulated in nonactivated T cells, and how the constitutively existing active forms of Lck are involved in a very efficient and fast signaling propagation upon ligation of TCR, are still open questions. And here, we wanted to examine whether and how CD4's spatial recruitment of Lck to the TCR plays a role in this puzzle.

So we examined the relative spatial distribution of Lck itself, and pairs of Lck–TCR and Lck–CD4 focusing on the active forms of Lck (Lck–pY394) using dSTORM. Recently, Gaus and coworkers used PALM and dSTORM to show that Lck clustering is dependent and tightly regulated by its conformation status (26). Our results for the clustering behavior of Lck–pY394 from our dSTORM imaging and the Ripley's *K*-function analysis agree well with their findings, in that active Lck forms exist preferentially in more clustered forms. They found that both the degree of clustering and the cluster sizes increase upon activation of T cells for the wild-type Lck. The fact that we did not observe this behavior is not surprising because we are only examining the Lck populations in their active conformation. And finally, a wide range of clustering and cluster sizes was also found in their mutated forms of Lck(Y505F) and Lck(Y505F, K273R), as we observed for the Lck–pY394 forms.

From dual-color imaging of nonactivated T cells for both Lck–TCR and Lck–CD4 pairs, we observed that the small clusters of TCR–CD3 or CD4 were still separate entities from the clusters of Lck–pY394. This observation fits with the view that key signaling molecules are segregated to better modulate their activity and suppress the nonspecific activation. And within 10 min of activation on LBL, TCR, CD4, and Lck molecules transported with macroscopic redistribution to develop well-organized IS, in which TCR clusters are located in the central area surrounded by CD4 and Lck clusters. In this type of mature IS, Lck molecules are also segregated away from TCR and CD4 molecules. However, how can this enhanced separation between critical components in T-cell signaling be compatible with T-cell activation? First, similar disparate accumulation of TCR and Lck has been reported for T cells interfacing antigen-presenting LBL (18) or APC (12, 45), and it was shown that Lck activity in proximity to the TCR is limited in the peripheral microclusters (18). As we could not observe newly generated TCR clusters in the periphery by either dSTORM or TIRFM, it was impossible to examine the nature of interactions between Lck and TCR in the previously suggested newly formed microclusters. However, if we combine our findings with the superresolution imaging data of T cells activated on immobilized surfaces coated with anti-CD3 antibodies by Gaus and coworkers (26), we can hypothesize that the separate nanoclusters of TCR and Lck in nonactivated cells concatenate upon the activation of T cells, while maintaining their separate structures, and that it is likely that Lck activities against TCR mainly occur in cluster–cluster interface.

For the same volume (or the surface area for a membrane-occupied entity) that a given number of molecules occupy, the size of the boundary surface (or the boundary line for a membrane-occupied entity), i.e., interface, is dependent upon how they are distributed. The smaller the cluster sizes, the bigger its interfaces. The small sizes of the preclusters of TCR guarantee the effective interfacial interactions with Lck. Furthermore, it was previously shown that Lck molecules alternate from being trapped within a CD2 cluster (with reduced mean diffusion coefficient of 0.26 $\mu m^2/s$) and being released to diffuse with a higher mean diffusion coefficient of 0.46 $\mu m^2/s$ (19). Therefore, the interfacial interactions would be sufficient to rapidly propagate signaling not only between the molecules trapped within each cluster but also between the protein clusters. Using dual-color PALM, Samelson and coworkers previously reported that LAT and TCR–CD3ζ clusters mainly colocalize at similar interfaces, and they postulated that these interfaces might serve as signaling "hot spots" (24). Interestingly, in the same report, they also showed that TCR–CD3ζ and ZAP-70 perfectly colocalize upon T-cell activation without forming the interfaces. As ZAP-70 is recruited to the phosphorylated CD3ζ chains upon T-cell activation (51), it is inferred that not only the TCR–CD3ζ molecules at the interfaces, but also the ones inside the clusters are effectively phosphorylated. Thus, it seems that the signaling within a TCR–CD3ζ cluster is propagated in a rapid and efficient manner. The difference in colocalization behaviors between the pairs of TCR and Lck or LAT (colocalize at interfaces) and the pair of TCR and ZAP-70 (colocalize without forming interfaces) might originate from the differences in their nature of association to the plasma membrane and the local membrane lipid compositions.

Within 5 min after activation, while actin-dependent transport of TCR clusters develops centrally concentrated SMAC, the cluster sizes become bigger, leaving Lck clusters surrounding the centrally located TCR clusters with regulated interfacial surfaces. Whether the resulting interfacial surfaces function to modulate signaling or as a more stabilized signaling hot spot awaits further investigation. It was also interesting to find that the Lck and CD4 clusters accumulating around TCR–CD3 in the cSMAC also maintain their disparate cluster structures. This observation is different from the colocalization of CD4 and Lck observed in T-cell–APC interfaces before (45). This discrepancy might simply be due to the significant differences in spatial resolution. In another observation made in T-cell–APC interface where the specific population of active Lck–pY394 is studied, they found that CD4 is critical for the recruitment of Lck molecules to IS between T-cell and APC for the initial 1–2 min, whereas CD28 is critical to potentiate and sustain Lck kinase activity afterward (12). Thus, it is possible to postulate that the spatial distribution of active Lck clusters in our results may represent the later stage of Lck clusters with coexisting CD28 molecules instead of the initial CD4-associated clusters. And the accumulation of CD28 microclusters in a spatially disparate subregion of cSMAC was also shown previously (52). Thus, it now seems that the structure of the IS is far more complex than previously appreciated.

In summary, CD4, active Lck (Lck–pY394), and TCR were preclustered in spatially separate protein islands/nanoclusters regardless of the activation state of the T cells, and in our experiments, these different entities were never fully colocalized (Fig. S12). The redistribution and enhancement in clustering of TCR and CD4 upon T-cell activation confine their interactions to the interfaces between clusters. It is important to note that we might possibly have failed to capture some short temporal window when these clusters fully integrate. However, this seems unlikely, as these separate clusters of protein are so ubiquitous. And as long as they contact at the interfaces, there will be quite a bit of possible interaction, given the speed of diffusion. Nevertheless, these spatially separate clusters effectively prevent nonspecific random initiation and propagation of signaling. And CD4–Lck interactions seem to play a significant role in the recruitment of Lck molecules into the IS between the T cell and APC. Once Lck molecules reach the IS, the active conformations could reside in their separate clusters, possibly colocalized with CD28, where they interact with TCR–CD3 complex molecules at the cluster interfaces. The separate clustering behaviors of TCR, CD4, and Lck molecules and their spatial redistribution forming a complex hierarchy in the IS suggest that this is not only a general property of T-cell signaling molecules, but likely other cell types as well.

Materials and Methods

Cells and Reagents. The 5c.c7 primary T blast cells were isolated from lymph nodes of transgenic mice and used in ∼7–10 d after being killed. The retroviral infections for the live cell PALM experiments were performed as described previously (21). Constructs of either PSCFP2 (Evrogen) or PAmCherry (mutagenesis of mCherry using a Stratagene kit) were introduced at the 3′ end of murine CD4 cDNA following sequences for 3(GGGGS) linker (Fig. S1*A*) in a murine stem cell virus-based retroviral vector and used to produce ecotropic retrovirus in Phoenix cells. For dual-color PALM, T2A sequence was incorporated in the same ORF between the constructs for CD3–PSCFP2 and CD4–PAmCherry (Fig. S1*B*). Poly-L-lysine, glucose oxidase, catalase, Triton-X, 2-mercaptoethanol (Sigma-Aldrich), streptavidin (Thermo Scientific), all lipids (Avanti), 16% (wt/vol) formaldehyde solution (Pierce), 8% (wt/wt) glutaldehyde (Electron Microscopy Sciences) were purchased and used as received. Anti-CD3ε–AF647 (clone: 145–2C11) and anti-CD4–AF647 (clone: RM4-5) antibodies were purchased from BioLegend. Polyclonal rabbit anti-Lck–pY394 antibody and secondary antibody against anti-rabbit IgG–AF488 were purchased from Bioss and Invitrogen, respectively. Biotinylated PLL was prepared by reaction of PLL with Sulfo NHS-LC-biotin (Pierce) in a targeted ratio of 1 biotin group for every 50 lysine units, followed by dialysis and lyophilization. IE^k–MCC, B7.1, and ICAM-1 with C-terminal 12His-tag and biotinylation motif were expressed in either bacteria (BL-21) or baculovirus-insect cell expression system (Sf9, Hi-5), and purified by Ni-NTA affinity chromatography (Qiagen) and size exclusion chromatography (Superdex200, GE Healthcare). Proteins used for the modification of immobilized surfaces were biotinylated using BirA (Avidity).

Preparation of Immobilized Surfaces and Glass Supported Lipid Bilayers. Immobilized surfaces were prepared by incubation of Lab-Tek eight-chambered coverglass (Nunc) with 200 μg/mL of either PLL or biotinylated PLL in distilled water for 1 h. For nonactivating surfaces, the chamber was washed three times with PBS and exchanged with the imaging buffer [HBSS with Ca^{2+} and Mg^{2+}, 2% (vol/vol) FCS] or complete RPMI 1640 before PALM or dSTORM experiments, respectively. For activating surfaces, the biotin–PLL surfaces were blocked with 2% (wt/vol) BSA in PBS for 30 min and further incubated with 50 μg/mL of streptavidin in the same blocking buffer for 30 min. After rigorous washing with PBS, the surfaces were incubated with 5 μg/mL of biotinylated IE^k–MCC and 8 μg/mL of biotinylated B7.1 for 30 min followed by washing with the imaging buffer for PALM experiments. For the preparation of glass-supported lipid bilayers, liposomes were prepared first. Chloroform solutions of 1-palmitoyl-2-oleoyl-sn-glycero-3-phosphocholine (POPC) and 1,2-dioleoyl-sn-glycero-3-[(*N*-(5-amino-1-carboxypentyl)iminodiacetic acid)succinyl](nickel salt) (DOGS-Ni-NTA) were mixed in 9:1 molar ratio in a round flask, and completely dried under vacuum overnight. The dried lipid mixture was resuspended in PBS at 2 mg/mL. Liposome was made by extrusion of the lipids suspension through a Mini-Extruder (Avanti) equipped with a Nuclepore track-etched polycarbonate membrane with 1-μm pore size (Whatman). Glass slides (Fisher Scientific) were cleaned with a 1:1 mixture of concentrated sulfuric acid and 30% (wt/wt) hydrogen peroxide (Sigma-Aldrich) for 30 min, rigorously rinsed with distilled water, air dried, and attached to the wells of a Lab-Tek chamber with epoxy glue. Chambers were incubated with a 10-fold dilution of previously prepared liposomes for 10 min. Supported lipid bilayers were washed with PBS and incubated with His-tagged IE^k–MCC (3.7 μg/mL), B7.1 (0.4 μg/mL), and ICAM-1 (0.8 μg/mL) in PBS for 1 h. The chamber was washed with PBS and complete RPMI 1640 before dSTORM experiments.

Superresolution Microscopies. An inverted fluorescence microscope (Axiovert 200M, Zeiss) equipped with a 100×/1.46 N.A. α Plan Apochromat objective lens (440782-9800, Zeiss) was used for all imaging. Samples were illuminated in TIRF microscopy mode with a 488-nm argon laser (excitation for PSCFP2

and AF488, Stabilite 2017-AR, Spectra Physics) in a combination with a 568-nm optically pumped semiconductor laser (excitation for PAmCherry, Sapphire 568, Coherent) or a 647-nm krypton laser (excitation for AF647, Stabilite-KR; Spectra Physics) line. A 405-nm UV diode laser (Radius405, Coherent) was applied in epifluorescence mode for accelerated photo-conversion rates. The fluorescence emission was separated with a dichroic mirror (585dcxr or 630dcxr, Chroma) installed in a beam splitter (DV2, Photometrics), and optically filtered with an et525/50m (PSCFP2, AF488) in combination with an et620/60m (PAmCherry) or a HQ680/50m (AF647) emission filter (Chroma). The StopLine Notch filter (Semrock) corresponding to each laser line was also used to prevent the excitation lights from being acquired. The samples were continuously photo-converted and excited, while stream acquisitions of images were performed by a back-illuminated electron multiplying charge coupled device (EMCCD) camera (Cascade II:512, Roper Scientific) at a readout speed of 5 MHz with full electron multiplying (EM) gain. For the live cell PALM, the cells in HBSS containing 2% (vol/vol) FBS were loaded onto the chamber on top of a temperature-controlled (37 °C) objective lens. Within ∼5–15 min after loading, images were acquired at an ∼4- to 10-ms frame rate for ∼1,000–3,000 frames. Using optimal excitation laser powers in the ranges of 0.3–1.5 kW/cm^2 for 488-nm argon laser (PSCFP2) and 0.1–0.6 kW/cm^2 for 568-nm laser (PAmCherry) and nonreducing imaging medium without oxygen scavenger, most of the PSCFP2 and PAmCherry molecules were irreversibly photobleached after initial excitation (30, 31), which minimized the blinking (38). The intensity of the 405-nm laser was optimized to maximize the number of visually distinguishable fluorophores appearing per frame.

For the dSTORM, the cells in culture medium (complete RPMI) were loaded onto the chamber and incubated in a CO_2 tissue culture incubator. In 10 min after loading, the cells in the chamber were sequentially washed with PBS, fixed with 4% (vol/vol) formaldehyde and 0.2% (vol/vol) glutaldehyde in PBS for 30 min, washed and blocked with 1% (vol/vol) FBS and 0.5% (wt/vol) BSA in PBS, and permeabilized with 0.5% (vol/vol) Triton-X in PBS. After incubations with antibodies for labeling and rigorous washings, the chamber was exchanged with an oxygen scavenging buffer (50 mM Tris, 10 mM NaCl, 143 mM 2-mercaptoethanol, 10% (wt/vol) glucose, 0.56 mg/mL glucose oxydase, 40 μg/mL catalase) for dSTORM imaging. The images were acquired at an ∼20- to 50-ms frame rate for ∼5,000–20,000 frames. The control experiments for correction of stage drift and precise overlay of dual-color images were performed using the 100-nm microspheres (TetraSpeck, Molecular Probes). The error associated with the alignment of dual-color images was calculated using more than five reference points near the four corners and a center of a rectangular acquisition window. The misplacements in all reference points were less than 0.1 CCD camera pixel distance (∼16 nm). Thus, the estimated overall positional accuracies in the dual-color PALM and STORM images are ∼40–50 nm. All of the device controls and image acquisitions were performed by using Metamorph software (Molecular Devices).

Data Analyses. PALM and dSTORM data were analyzed using custom software written in MATLAB (MathWorks) for single molecular localization by Gaussian approximation of the microscope's optical point spread function and maximum-likelihood algorithm (21), and the positional accuracy for each single molecule was determined (53). Rigorous filtration for the signals determined as a single molecule was followed using strict thresholds applied for signal-to-noise ratio, intensity, full width at half maximum, and the positional accuracy. Furthermore, all of the signals located within the same pixel in consecutive frames were discarded except the first frame of the particular series. The reconstructions of PALM and dSTORM images were also performed using MATLAB (MathWorks). For the single-color experiments, color maps of density distribution of molecules were created by representing each molecule by a normalized Gaussian density distribution function with a width given by the determined positional accuracy determined in the localization of the particular fluorophore. For the dual-color experiments, each molecule was represented by a circle in green or red with a radius equal to the mean positional accuracy. In the reconstituted two-color PALM and dSTORM images, the yellow pixels represent the area where the green and red circles overlay. The spatial distributions of molecules were analyzed using Ripley's *K* function and bivariate pair correlation function analyses. Typically, representative 3 × 3 μm^2 areas per cell were used for a single analysis, and all of the analyses were performed for every 5-nm increment up to 1 μm addressing edge effects. For single-color data, 100 Monte Carlo simulations of Ripley's *K*-function analyses using randomized datasets were performed to achieve 99% confidence intervals, and positive deviation in L(*r*) minus *r* values from the upper confidence line indicated a statistically significant clustered behavior. For bivariate pair-correlation function analyses of two-color data, we used a random labeling model as a null hypothesis. In this model, all of the molecules are randomly labeled for a given number of molecules per type (determined by the sample), while locations of all of the molecules are preserved. Again, 100 simulations were performed to achieve 95% confidence intervals. The negative deviation of the data line from the lower confidence line indicated a statistically segregated behavior compared with random labeling. Univariate or bivariate nearest neighbor analyses were performed by calculating the fraction of CD4 molecules that have at least either a neighboring CD4 molecule (univariate) or a neighboring TCR–CD3 molecule (bivariate) within varying distances. The distance up to which the PALM data show positive deviation from the values calculated for the randomized case (Monte Carlo method) was determined either as a radius of a hypothetically circular nanocluster or as a distance over which CD4 and TCR–CD3 clusters overlap. The detected number of molecules within a hypothetically circular cluster was adjusted to the reported number of molecules by normalization with the detection rate of molecules in PALM. It was estimated that only 45–75% of the total CD4 molecules and 37–55% of the total TCR–CD3 molecules could be recognized in PALM. For this estimation, it was assumed that the actual total numbers of CD4 and TCR–CD3 molecules are 5 × 10^4 (54, 55) and 1 × 10^5 (56, 57), respectively, per cell with a size of 10 μm in diameter. The degree of mixing parameter was introduced and calculated as this: First, the ratio between the g_{12} value of the sample and the mean value of g_{12} from 100 random labeling simulations were calculated. Then, the averaged value of these ratios up to 100 nm was determined as degree of mixing. Linescan analysis of TIRFM images was performed using Metamorph software (Molecular Devices).

ACKNOWLEDGMENTS. We thank Salvatore Valitutti and Cristina Tato for critical reading of the manuscript and Michael Kuhns for the CD4 construct. This work was funded by Grant R01AI055211-30 from the National Institutes of Health and by the Howard Hughes Medical Institute.

1. Marrack P, et al. (1983) The major histocompatibility complex-restricted antigen receptor on T cells. II. Role of the L3T4 product. *J Exp Med* 158(4):1077–1091.
2. Hampl J, Chien YH, Davis MM (1997) CD4 augments the response of a T cell to agonist but not to antagonist ligands. *Immunity* 7(3):379–385.
3. Madrenas J, Chau LA, Smith J, Bluestone JA, Germain RN (1997) The efficiency of CD4 recruitment to ligand-engaged TCR controls the agonist/partial agonist properties of peptide-MHC molecule ligands. *J Exp Med* 185(2):219–229.
4. Irvine DJ, Purbhoo MA, Krogsgaard M, Davis MM (2002) Direct observation of ligand recognition by T cells. *Nature* 419(6909):845–849.
5. König R, Huang LY, Germain RN (1992) MHC class II interaction with CD4 mediated by a region analogous to the MHC class I binding site for CD8. *Nature* 356(6372):796–798.
6. Cammarota G, et al. (1992) Identification of a CD4 binding site on the beta 2 domain of HLA-DR molecules. *Nature* 356(6372):799–801.
7. Janeway CA, Jr (1992) The T cell receptor as a multicomponent signalling machine: CD4/CD8 coreceptors and CD45 in T cell activation. *Annu Rev Immunol* 10:645–674.
8. Huppa JB, et al. (2010) TCR-peptide-MHC interactions in situ show accelerated kinetics and increased affinity. *Nature* 463(7283):963–967.
9. Turner JM, et al. (1990) Interaction of the unique N-terminal region of tyrosine kinase p56lck with cytoplasmic domains of CD4 and CD8 is mediated by cysteine motifs. *Cell* 60(5):755–765.
10. Straus DB, Weiss A (1992) Genetic evidence for the involvement of the lck tyrosine kinase in signal transduction through the T cell antigen receptor. *Cell* 70(4): 585–593.
11. Li QJ, et al. (2004) CD4 enhances T cell sensitivity to antigen by coordinating Lck accumulation at the immunological synapse. *Nat Immunol* 5(8):791–799.
12. Holdorf AD, Lee KH, Burack WR, Allen PM, Shaw AS (2002) Regulation of Lck activity by CD4 and CD28 in the immunological synapse. *Nat Immunol* 3(3):259–264.
13. Vidal K, Daniel C, Hill M, Littman DR, Allen PM (1999) Differential requirements for CD4 in TCR-ligand interactions. *J Immunol* 163(9):4811–4818.
14. Grakoui A, et al. (1999) The immunological synapse: A molecular machine controlling T cell activation. *Science* 285(5425):221–227.
15. Monks CRF, Freiberg BA, Kupfer H, Sciaky N, Kupfer A (1998) Three-dimensional segregation of supramolecular activation clusters in T cells. *Nature* 395(6697):82–86.
16. Seminario MC, Bunnell SC (2008) Signal initiation in T-cell receptor microclusters. *Immunol Rev* 221:90–106.
17. Yokosuka T, et al. (2005) Newly generated T cell receptor microclusters initiate and sustain T cell activation by recruitment of Zap70 and SLP-76. *Nat Immunol* 6(12): 1253–1262.
18. Campi G, Varma R, Dustin ML (2005) Actin and agonist MHC-peptide complex-dependent T cell receptor microclusters as scaffolds for signaling. *J Exp Med* 202(8):1031–1036.
19. Douglass AD, Vale RD (2005) Single-molecule microscopy reveals plasma membrane microdomains created by protein-protein networks that exclude or trap signaling molecules in T cells. *Cell* 121(6):937–950.
20. Bunnell SC, et al. (2002) T cell receptor ligation induces the formation of dynamically regulated signaling assemblies. *J Cell Biol* 158(7):1263–1275.
21. Lillemeier BF, et al. (2010) TCR and Lat are expressed on separate protein islands on T cell membranes and concatenate during activation. *Nat Immunol* 11(1):90–96.

22. Lillemeier BF, Pfeiffer JR, Surviladze Z, Wilson BS, Davis MM (2006) Plasma membrane-associated proteins are clustered into islands attached to the cytoskeleton. *Proc Natl Acad Sci USA* 103(50):18992–18997.
23. Kumar R, et al. (2011) Increased sensitivity of antigen-experienced T cells through the enrichment of oligomeric T cell receptor complexes. *Immunity* 35(3):375–387.
24. Sherman E, et al. (2011) Functional nanoscale organization of signaling molecules downstream of the T cell antigen receptor. *Immunity* 35(5):705–720.
25. Williamson DJ, et al. (2011) Pre-existing clusters of the adaptor Lat do not participate in early T cell signaling events. *Nat Immunol* 12(7):655–662.
26. Rossy J, Owen DM, Williamson DJ, Yang Z, Gaus K (2013) Conformational states of the kinase Lck regulate clustering in early T cell signaling. *Nat Immunol* 14(1):82–89.
27. Betzig E, et al. (2006) Imaging intracellular fluorescent proteins at nanometer resolution. *Science* 313(5793):1642–1645.
28. Rust MJ, Bates M, Zhuang X (2006) Sub-diffraction-limit imaging by stochastic optical reconstruction microscopy (STORM). *Nat Methods* 3(10):793–795.
29. van de Linde S, et al. (2011) Direct stochastic optical reconstruction microscopy with standard fluorescent probes. *Nat Protoc* 6(7):991–1009.
30. Chudakov DM, et al. (2004) Photoswitchable cyan fluorescent protein for protein tracking. *Nat Biotechnol* 22(11):1435–1439.
31. Subach FV, et al. (2009) Photoactivatable mCherry for high-resolution two-color fluorescence microscopy. *Nat Methods* 6(2):153–159.
32. Seder RA, Paul WE, Davis MM, Fazekas de St Groth B (1992) The presence of interleukin 4 during in vitro priming determines the lymphokine-producing potential of CD4+ T cells from T cell receptor transgenic mice. *J Exp Med* 176(4):1091–1098.
33. de Felipe P, et al. (2006) E unum pluribus: Multiple proteins from a self-processing polyprotein. *Trends Biotechnol* 24(2):68–75.
34. Donnelly MLL, et al. (2001) Analysis of the aphthovirus 2A/2B polyprotein 'cleavage' mechanism indicates not a proteolytic reaction, but a novel translational effect: a putative ribosomal 'skip'. *J Gen Virol* 82(Pt 5):1013–1025.
35. Mascalchi P, Lamort AS, Salomé L, Dumas F (2012) Single Particle Tracking reveals two distinct environments for CD4 receptors at the surface of living T lymphocytes. *Biochem Biophys Res Commun* 417(1):409–413.
36. Favier B, Burroughs NJ, Wedderburn L, Valitutti S (2001) TCR dynamics on the surface of living T cells. *Int Immunol* 13(12):1525–1532.
37. Shroff H, Galbraith CG, Galbraith JA, Betzig E (2008) Live-cell photoactivated localization microscopy of nanoscale adhesion dynamics. *Nat Methods* 5(5):417–423.
38. Sengupta P, et al. (2011) Probing protein heterogeneity in the plasma membrane using PALM and pair correlation analysis. *Nat Methods* 8(11):969–975.
39. Krummel MF, Sjaastad MD, Wülfing C, Davis MM (2000) Differential clustering of CD4 and CD3zeta during T cell recognition. *Science* 289(5483):1349–1352.
40. Palacios EH, Weiss A (2004) Function of the Src-family kinases, Lck and Fyn, in T-cell development and activation. *Oncogene* 23(48):7990–8000.
41. Xu H, Littman DR (1995) The kinase-dependent function of Lck in T-cell activation requires an intact site for tyrosine autophosphorylation. *Ann N Y Acad Sci* 766:99–116.
42. Alonso A, et al. (2004) Lck dephosphorylation at Tyr-394 and inhibition of T cell antigen receptor signaling by Yersinia phosphatase YopH. *J Biol Chem* 279(6):4922–4928.
43. Nika K, et al. (2010) Constitutively active Lck kinase in T cells drives antigen receptor signal transduction. *Immunity* 32(6):766–777.
44. Varma R, Campi G, Yokosuka T, Saito T, Dustin ML (2006) T cell receptor-proximal signals are sustained in peripheral microclusters and terminated in the central supramolecular activation cluster. *Immunity* 25(1):117–127.
45. Ehrlich LIR, Ebert PJR, Krummel MF, Weiss A, Davis MM (2002) Dynamics of p56lck translocation to the T cell immunological synapse following agonist and antagonist stimulation. *Immunity* 17(6):809–822.
46. Zhong L, et al. (2009) NSOM/QD-based direct visualization of CD3-induced and CD28-enhanced nanospatial coclustering of TCR and coreceptor in nanodomains in T cell activation. *PLoS ONE* 4(6):e5945.
47. Shaw AS, et al. (1989) The lck tyrosine protein kinase interacts with the cytoplasmic tail of the CD4 glycoprotein through its unique amino-terminal domain. *Cell* 59(4):627–636.
48. Glaichenhaus N, Shastri N, Littman DR, Turner JM (1991) Requirement for association of p56lck with CD4 in antigen-specific signal transduction in T cells. *Cell* 64(3):511–520.
49. Paster W, et al. (2009) Genetically encoded Förster resonance energy transfer sensors for the conformation of the Src family kinase Lck. *J Immunol* 182(4):2160–2167.
50. Stirnweiss A, et al. (2013) T cell activation results in conformational changes in the Src family kinase Lck to induce its activation. *Sci Signal* 6(263):ra13.
51. Wang H, et al. (2010) ZAP-70: An essential kinase in T-cell signaling. *Cold Spring Harb Perspect Biol* 2(5):a002279.
52. Yokosuka T, et al. (2008) Spatiotemporal regulation of T cell costimulation by TCR-CD28 microclusters and protein kinase C theta translocation. *Immunity* 29(4):589–601.
53. Thompson RE, Larson DR, Webb WW (2002) Precise nanometer localization analysis for individual fluorescent probes. *Biophys J* 82(5):2775–2783.
54. Poncelet P, et al. (1991) Surface CD4 density remains constant on lymphocytes of HIV-infected patients in the progression of disease. *Res Immunol* 142(4):291–298.
55. Hultin LE, Matud JL, Giorgi JV (1998) Quantitation of CD38 activation antigen expression on CD8+ T cells in HIV-1 infection using CD4 expression on CD4+ T lymphocytes as a biological calibrator. *Cytometry* 33(2):123–132.
56. Matsui K, et al. (1991) Low affinity interaction of peptide-MHC complexes with T cell receptors. *Science* 254(5039):1788–1791.
57. Sykulev Y, et al. (1994) Kinetics and affinity of reactions between an antigen-specific T cell receptor and peptide-MHC complexes. *Immunity* 1(1):15–22.